Electron Tomography of Ice-Embedded Prokaryotic Cells

Rudo Grimm,* Hapreet Singh,* Reinhard Rachel,# Dieter Typke,* Wolfram Zillig,* and Wolfgang Baumeister*
*Max-Planck-Institut für Biochemie, 82152 Martinsried, and #Universität Regensburg, 93053 Regensburg, Germany

ABSTRACT Whole cells of archaea were embedded in vitreous ice by plunge freezing and investigated by automated energy-filtered electron tomography at 120 kV. The embedded cells were between 300 and 750 nm thick, and their structures were reconstructed to a resolution of 20–40 nm from tilt series comprising 50–140 images. The dose was kept within tolerable limits. A resolution of 20 nm allowed visualization of the individual stalks of the S-layer of *Pyrobaculum aerophilum* cells, which had undergone partial lysis, in three dimensions. The attainable resolution for low-dose electron tomography under different experimental conditions was theoretically investigated in terms of the specimen thickness. To obtain 2-nm resolution at 120 kV (300 kV), the specimen must not be thicker than 100 nm (150 nm). For a resolution of 10 nm, the maximum thickness is 450 nm (700 nm). An accelerating voltage of 300 kV is advantageous, mainly for specimens thicker than 100 nm. Experimental investigations so far have resulted in a resolution that is worse by a factor of 2–5 as compared to theory.

INTRODUCTION

Electron tomography allows the three-dimensional investigation of structures over a wide range of sizes, from cellular structures to single macromolecules. It has recently been applied to the study of stained sections of mitochondria (Mannella et al., 1994; Perkins et al., 1997), centrosomes (Moritz et al., 1995), and secretion organelles (Shillito et al., 1997). In contrast to resin embedding and sectioning, preparation in amorphous ice yields a better preservation of the native state of biological samples. In principle, the interpretation is also more straightforward, because in stained samples it is unclear—at least on the molecular scale—how the stain distribution relates to the underlying biological structure. However, specimen contrast in amorphous ice is much lower, and the total electron dose is limited to roughly $2000-6000$ e nm^{-2} because of the radiation sensitivity of the ice-embedded samples. Radiation damage results in structural changes on the molecular level and at higher dose in bubble formation. Electron tomography ensures that this dose is used efficiently by applying it to a three-dimensional image instead of a mere projection (McEwen et al., 1995). To use most of the allowed dose for the actual image acquisition, tomographic procedures have to be highly automated (Koster et al., 1992; Dierksen et al., 1992, 1993; Braunfeld et al., 1994). This means that focusing and tracking of the sample during the tilt series have to be performed by computer control, at positions different from the actual region of interest. In this way it was possible to study virus particles (Dierksen et al., 1993), lipid vesicles with or without cargo (Dierksen et al., 1995; Grimm et al., 1997), and macromolecules (Nitsch et al., manuscript submitted for publication).

Energy filtering improves image contrast by selecting electrons within a narrow energy window, thereby minimizing the loss of resolution and contrast due to chromatic aberration (Schröder et al., 1990; Langmore and Smith, 1992; Grimm et al., 1996a). If applied to thick stained sections, it can be used to image the most probable energy loss, which can also be exploited in electron tomography (Olins et al., 1989). When ice-embedded specimens are investigated, the best contrast and resolution are generally achieved by selecting the zero-loss electrons for imaging (Grimm et al., 1996b).

In the first section of this paper we will present recent results of tomography of ice-embedded whole cells of archaea. The long-term goal of these studies is the detection of macromolecular structures in their native context, i.e., in their cellular environment (we have previously used a system of actin and vesicles to study the feasibility of this aim for dilute samples; Grimm et al., 1997). In a second section, considerations of the resolution that can be obtained in a tomographic reconstruction under low-dose conditions are presented. The calculations include the number of required images for a given resolution, the exposure time required for statistically significant images, and the effect of increasing specimen thickness.

MATERIALS AND METHODS

Sulfolobus cells (Brock et al., 1972; Schleper et al., 1995) were taken directly from stock solutions at an OD between 0.3 and 0.7, applied to a holey carbon grid, and plunge-frozen in liquid ethane (Dubochet et al., 1988). Cells of *Pyrobaculum aerophilum* were first concentrated by centrifugation before application to the grid (Völkl et al., 1993).

Electron microscopy was performed on a Philips CM 120 Biofilter (Philips E.O., Eindhoven, The Netherlands) with a post-column energy filter (Krivanek et al., 1995; de Jong et al., 1996). The goniometer (Compustage) was fully accessible to external computer control. The accelerating voltage was 120 kV. The magnification was 6200× or 14,500× on the CCD camera (pixel size 24 μm). Tracking of the specimen during tomography was done at 6200× magnification. By further developing the software used in previous experiments (Grimm et al., 1997), the programs for electron tomography were fully automated and implemented in the soft-

Received for publication 25 September 1997 and in final form 11 November 1997.

Address reprint requests to Dr. Dieter Typke, MPI Biochemie, Molekulare Strukturbiologie, 82152 Martinsried, Germany. Tel.: +49-89-85782620; Fax: +49-89-857826411; E-mail: typke@biochem.mpg.de.

0006-3495/98/02/1031/12 $2.00

ware package Digital Micrograph (Gatan, Pleasanton, CA) on a Macintosh 8500 computer. The reconstructions were computed by weighted back-projection with the EM software package (Hegerl, 1996), with an image alignment using 10-nm colloidal gold particles added to the specimen.

RESULTS

The gain in resolution in the investigation of cells with a diameter of 0.5–1 μm by zero-loss energy filtering (i.e., removal of the inelastically scattered electrons) is illustrated in Fig. 1. The *Sulfolobus* cell is fully embedded in vitreous ice. The indicated thickness of the ice in Fig. 1 *B* corresponds to the local height of the cell. Energy filtering drastically improves the resolution and contrast of the image, so that the S-layer as well as some large structures inside the cell become visible. Because of the nonuniform thickness of the specimen, the count rate varies between 1 (35) and 200 (230) e/pixel in the filtered (unfiltered) image. When tilting, it is only possible to keep the count rate and thereby the signal-to-noise ratio (SNR) of one area of a given thickness constant for all angles by adjusting the exposure time according to $t = t_0\exp[T(\cos^{-1}\alpha - 1)]$ (tilt angle α, specimen thickness in terms of the mean free path T). As the image intensity decreases exponentially with the thickness of the specimen, and the thickness changes as $1/\cos\alpha$, the above scheme will result in a constant image intensity over the full tilt range for a specimen of homogeneous thickness and density. If the specimen thickness varies, severe over- or underexposure is observed in the high-tilt images for those areas where the relative thickness differs strongly from T in the above equation. For the series presented below, we have chosen a variation with $t = t_0/\cos\alpha$ as a satisfactory compromise for $T \approx 1$ (see second section).

A tomographic reconstruction of a *Sulfolobus* cell is shown in Fig. 2. All reconstructions were computed using the logarithm of the original image intensities, corresponding to the contrast produced by the removal of inelastically scattered electrons. This allows the interpretation of image intensities in the reconstructed volume in terms of relative mass densities. Reconstruction using the original image intensities leads to well-defined fine structures but inaccurate low-resolution information, as observed by a strong radial density gradient through the cell and in the z direction (data not shown). To be able to correctly interpret the full image information, it would be necessary to separate the linear and nonlinear contrast contributions (Han et al., 1996). In principle, it would be possible to then reconstruct them independently. Because of the strong dose limitations and the comparatively low resolution of tomographic reconstructions of thick specimens, this is neither feasible nor worthwhile in our case. With 52 tilted images and a thickness of the cell of 750 nm at its thickest point, the reconstruction in Fig. 2 has a resolution in the z direction that is not better than 40 nm (see Eq. 1 below), with a higher resolution in the x-y plane and in the thin regions of the specimen. One can identify the cytoplasmic membrane (4 nm in width), the S-layer (~10 nm width), and the space in between, the (quasi-) periplasmic space (~20 nm wide) (Völkl et al., 1993). This space is thought to be functionally analogous to the periplasmic space of Gram-negative eubacteria and represents an extracellular compartment (Baumeister et al., 1989). The S-layer of the cell is partly discontinuous. Vesicles attached to the cell, a dense spherical "inclusion" in the cell, and a pilus (*marked by arrowheads*) are also observed.

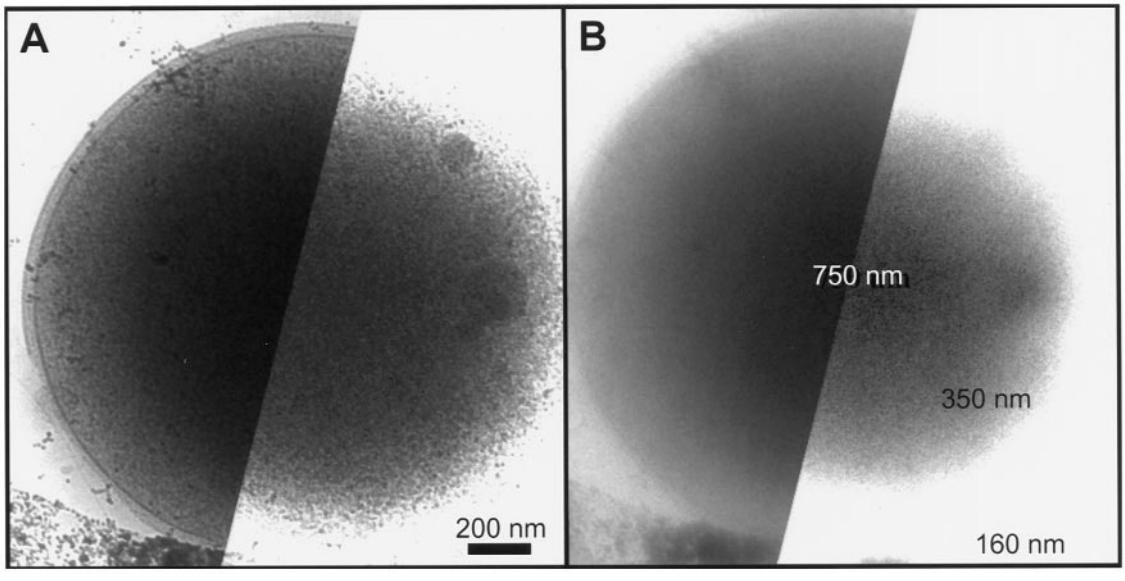

FIGURE 1 Images of a whole *Sulfolobus* HI15 PING cell in ice. (*A*) Zero-loss energy filtered image. (*B*) Unfiltered image. The images are divided into two halves with different scaling, to visualize the full dynamic range of the recorded data. Microscope magnification was 14,500×. The numbers in *B* indicate the local thickness of the cell, which is about equal to the thickness of the embedding ice layer.

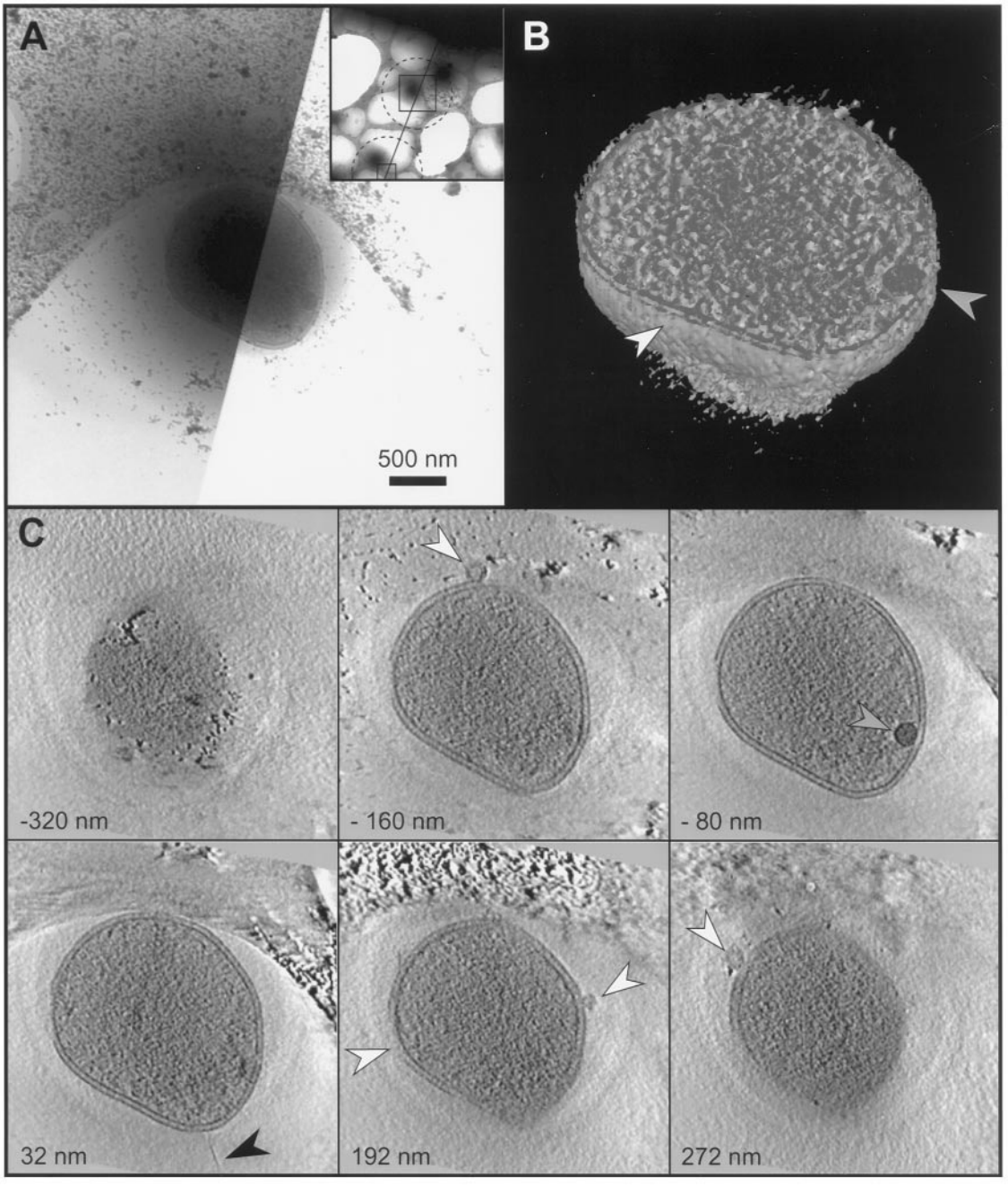

FIGURE 2 Tomographic reconstruction of a whole *Sulfolobus* HI15 PING cell, maximum thickness 750 nm. The series consisted of 52 images between 60° and −67.5° tilt angle with an evenly spaced increment of 2.5°. The total dose for the series was 6000*e* nm^{-2}. The magnification was 6200×. (*A*) Projection at 0° tilt angle. The image is divided into two halves with different scaling. The inset shows the positions used in electron tomography for imaging (*center*) and autofocusing (*bottom*) at an overview magnification. The direction of the tilt axis is indicated. (*B*) Lower half of the surface rendered reconstruction. The S-layer and a round structure within the cell are visible. (*C*) Sections (8 nm thick) from the reconstructed volume. The height in the *z* direction relative to the central section is indicated. Arrowheads point to features in the S-layer and to vesicles (*white*), to the electron-dense inner structure (*gray*), and to a pilus (*black*).

To obtain a higher resolution, it is necessary to distribute the dose of one series to more images. In higher-magnification tomography of single molecules, the lowest permissible dose per image is determined by the ability to align the individual images by image cross-correlation, eventually using high-contrast markers. In our case, the alignment is carried out using gold beads localized in the relatively thin ice film neighboring the cell. The dose per image is therefore determined by the requirement that the measured intensity on the CCD at the thickest part of the specimen, i.e., at the center of the cell, results in a sufficient SNR. An example of a cell with a nominal resolution of ~12 nm (139 images, 600 nm maximum thickness) is displayed in Fig. 3. The actual resolution, however, is worse than 20 nm, be-

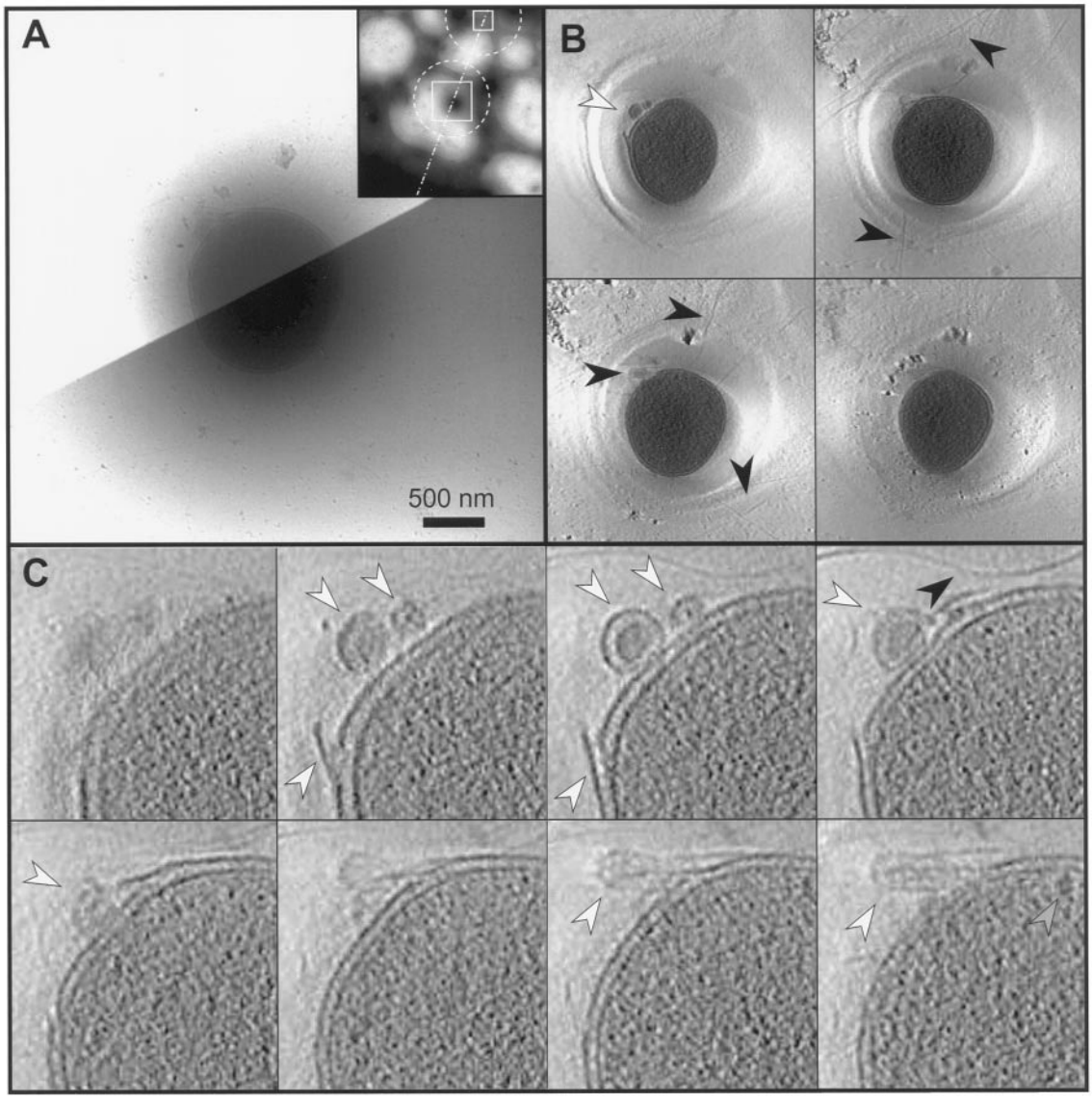

FIGURE 3 Tomographic reconstruction of a whole *Sulfolobus* NOB8H2 cell, maximum thickness 600 nm. The series consisted of 139 images between −64° and 50° with a variable tilt increment according to the scheme proposed by Saxton et al. (1984), starting with an increment of 1.1° at 0° tilt. The total dose was 7000*e* nm^{-2}. The magnification was 6200×. (*A*) 0° projection from the series (as in Fig. 2 *A*). (*B*) Sections (16 nm thick), 150 nm apart in the *z* direction, from the reconstructed volume. Pili (*black arrowheads*) and a small round structure (*white arrowhead*) are seen. (*C*) Details from the x-y sections (pixel size 8 nm). The individual sections are 8 nm thick and 40 nm apart. A damaged S-layer and budding (*white arrowheads*) and pili (*black arrowheads*) are observed. The gray arrowhead in the last image shows a distinct dark feature within the cell that can be identified when scanning through the stack in the *z* direction.

cause the periodicity of the S-layer lattice remains invisible (lattice spacing ~20 nm). Besides the identification of pili and discontinuities in the S-layer, this resolution allows the attached "vesicles" to be identified as budding protrusions, which are completely covered by an S-layer protein sheet. Within the densely filled cell, several smaller structures are barely observable when scanning through the *x-y* slices in the *z* direction. In addition, an unknown structure ~30–40 nm in size could be clearly singled out (*gray arrow in the last image*).

Because *Sulfolobus* cells appear to be too large to visualize macromolecular complexes inside them at 120 kV, the archaeon *Pyrobaculum*, with a diameter of only 400–500 nm, was chosen for further investigation. With a lattice spacing of the S-layer of ~30 nm (Völkl et al., 1993), this cell type is appropriate for demonstrating that the resolution of the reconstruction is at least better than this value. Fig. 4 shows a projection and slices from the reconstruction of a mostly empty *Pyrobaculum* cell. It is ~700 nm wide and 300 nm thick at its highest point around an enclosed structure of condensed cell contents. An investigation by elemental mapping (using the three-window method) of this structure, which was found in all cell ghosts, did not reveal a significantly increased concentration of phosphorus, as

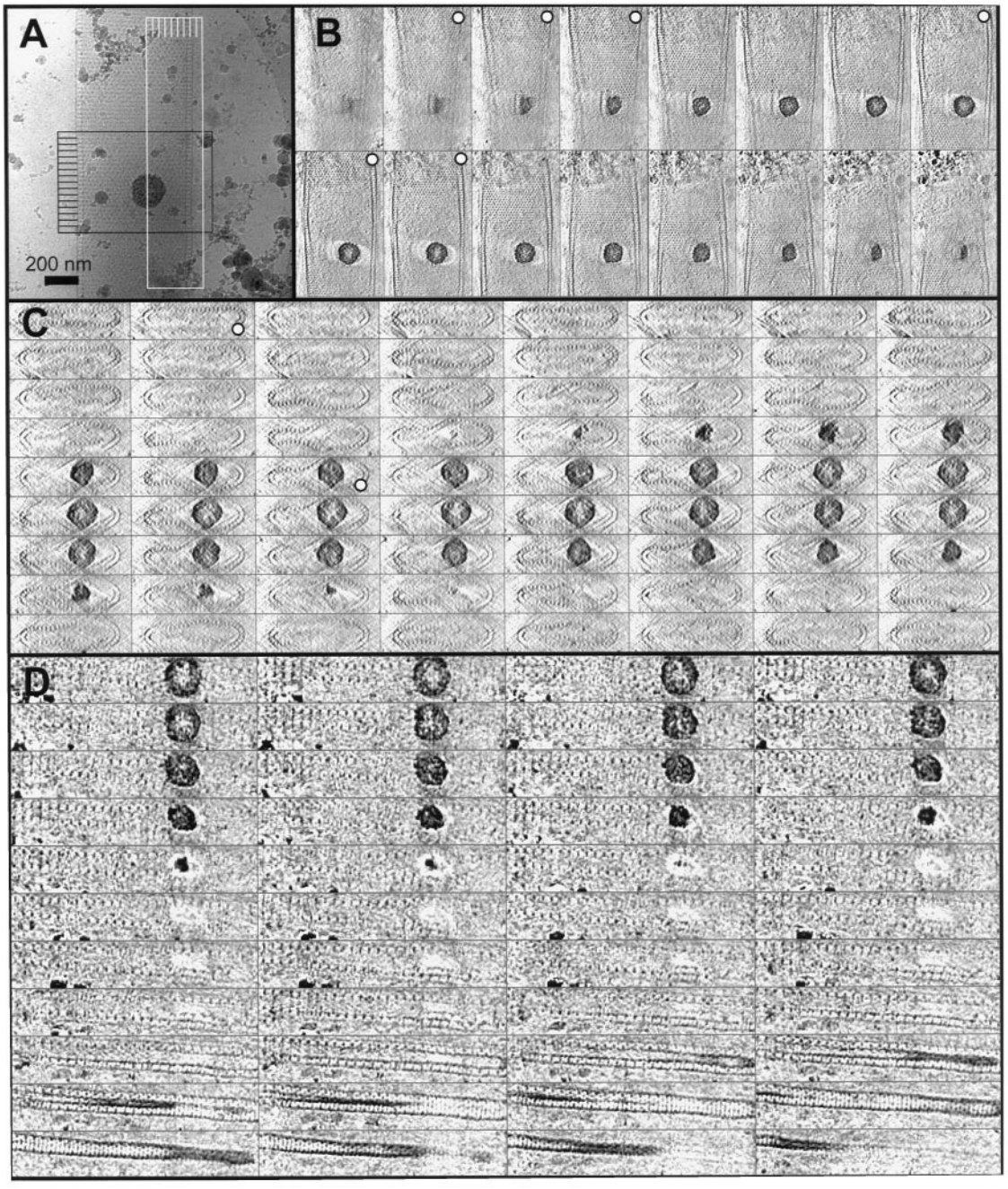

FIGURE 4 Reconstruction of a 300-nm-thick collapsed *Pyrobaculum* cell from 58 images in the range between −63° and 61°. The defocus was 33 μm, so that the first zero of the CTF was at about $(11\ \text{nm})^{-1}$. Magnification 14,500×, total dose $7000e\ \text{nm}^{-2}$. (*A*) Projection at 0° tilt. The area and direction of the sections shown in *C* and *D* are indicated in black and white, respectively. (*B*) Sections in the *x*-*y* plane. All sections are 8 nm thick. Only every other section is shown. One can observe a slight tilt of the cell about the *x* axis. The S-layer periodicity is readily visible on the top and bottom. (*C*) Sections in the *x*-*z* plane as indicated in *A*. Even though the membrane can only be followed at the edges, because of the missing wedge, the stalks of the S-layer can be seen in all directions. (*D*) *y*-*z* sections clearly showing the stalks on the top and bottom of the cell, and the stalks in the *x* direction at the edge. The periodicity of the S-layer is ~30 nm.

should be the case if the structure consisted of condensed DNA. The nominal resolution of the series was 15 nm, so that the defocus was set accordingly, with the first zero of the CTF at $(11\ \text{nm})^{-1}$, corresponding to about a quarter of the Nyquist frequency. The localization and orientation of S-layer stalks in a hexagonal lattice can be clearly identified in all sections. These stalks anchor the surface layer into the cell membrane, creating the (quasi-) periplasmic space (Phipps et al., 1990), which is 15–17 nm wide (Phipps et al., 1991). From Fig. 4 *B* one can infer that the cell is almost completely collapsed. At the top edge of the image, the upper layer (relative to the *z* direction) is visible in the second to fourth images of the first row, whereas the lower layer is seen in the last image of the top row and the first

two images of the second row (*round markers*). Fig. 4 *C* shows this flattening more clearly, especially in the first image. Near the enclosed spherical structure, the cross section is bottle-shaped, which is clearly seen in the marked image in the fifth row. Even though the membrane is only seen close to the edges because of the missing wedge, it can be traced by the fact that the stalks are always oriented perpendicular to it. Fig. 4 *D* clearly reveals the cross section of the stalks near the edge of the cell, where they are attached to the membrane.

A second reconstruction of a *Pyrobaculum* cell is shown in Fig. 5. Even though the cell appears to be intact (judging from the 0° projection), the reconstruction shows that it is in fact almost empty, and that the dark appearance of the cell in the projections is a thickness effect. The whole cell is 500 nm thick and not more compressed in the *z* direction than expected for intact cells. Fig. 5, *B* and *C*, shows *x*-*y* slices revealing the S-layer periodicity at the top (*C*) and bottom (*B*) of the cell. This periodicity was not visible in any of the projections. Fig. 5 *D* displays slices in the *x*-*z* plane, which reveal that the density is only slightly higher in the cell than in the embedding ice film. At the lower end of the cell, the cross sections of the stalks are again clearly seen. As the cell is oriented slightly diagonal in the volume, only a few stalks are seen in the *y*-*z* slices (data not shown). With almost twice as many projections, this reconstruction has the same nominal resolution as in Fig. 4, because of the larger thickness of the cell. The somewhat poorer visibility of the stalks

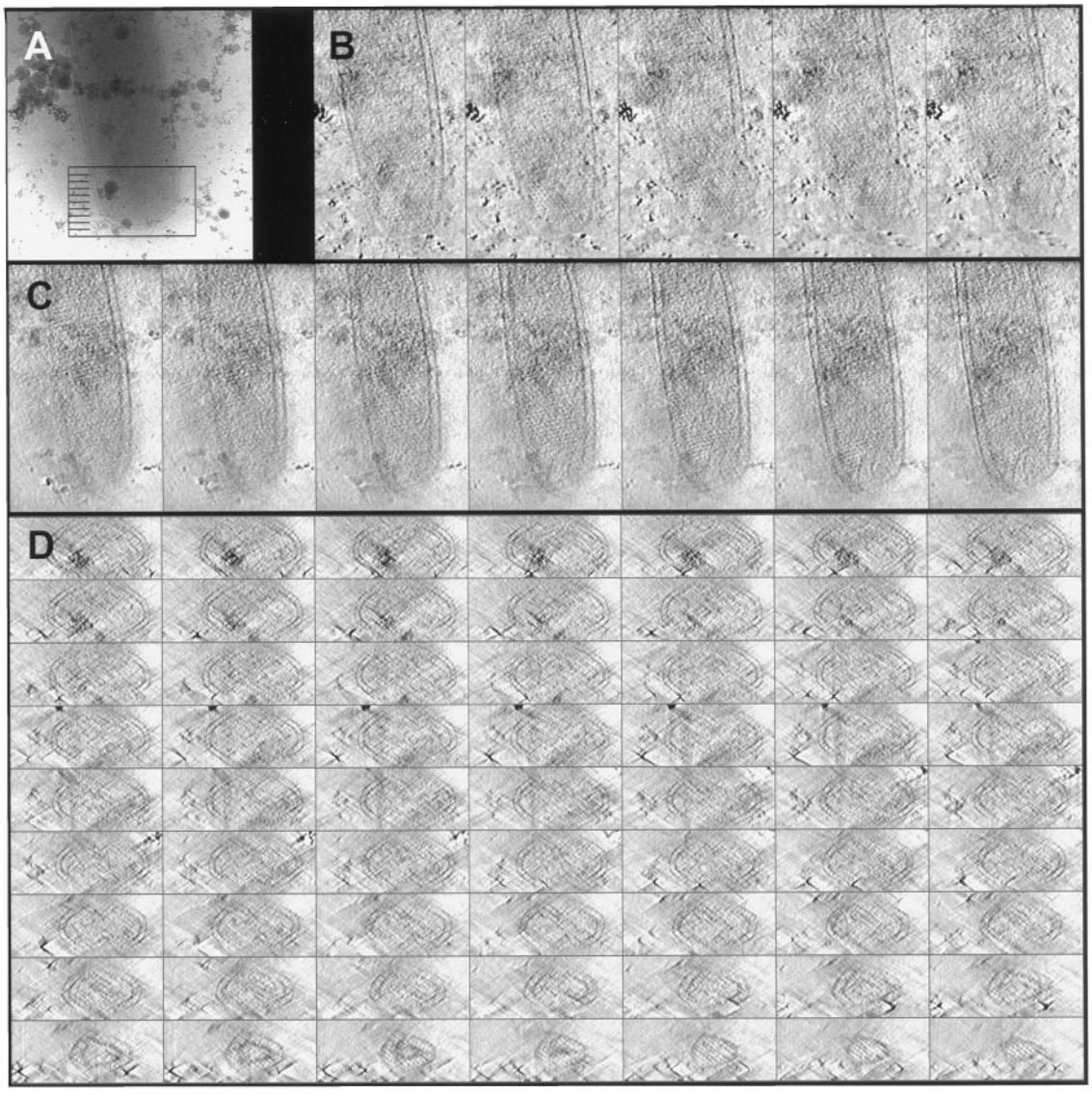

FIGURE 5 A whole 500-nm-thick *Pyrobaculum* cell that is only slightly compressed by the embedding ice layer, even though it appears empty upon close examination of the densities. Ninety-six images between ±60° were recorded. Because of the smaller defocus of 14 μm and the larger thickness, the contrast is less than in Fig. 4. Magnification 14,500×, total dose 11,000*e* nm^{-2}. Some visible beam damage occurred during the series. (*A*) 0° projection image. The area and direction of the sections in *D* are indicated. (*B*) *x*-*y* sections at the top of the cell. (*C*) *x*-*y* sections at the bottom of the cell. The periodicity of the S-layer is visible. (*D*) Sections in the *x*-*z* plane. Note the weak deformation of the cell, the readily visible membranes, and cross sections of the S-layer stalks at the tip of the cell.

is due to the smaller defocus (14 μm versus 33 μm). It is obvious that the low contrast of ice-embedded structures poses a limitation for this type of tomography, which cannot use averaging as a remedy.

DISCUSSION

Whole cells of the archaeon *Sulfolobus*, with a diameter of ~1 μm, were embedded in vitreous ice. Flattening to ~600 nm occurred because of the surface tension of the solution during preparation of the thin ice films. The structure of the cells was investigated in three dimensions by electron tomography, with a resolution of 20–40 nm. The nature of the large round structure inside the cytoplasm of the cell in Fig. 2 *C* is not known. It is spherical, with a diameter of 150 nm, and is significantly more dense than the cytoplasm on average. We assume it to be a densely packed inclusion body of unknown composition. We have found structures of similar size, sometimes more than one (e.g., in Fig. 1), in many other cells of the same species. In projection images it is not possible to distinguish them from contaminating round ice crystals, so that tomography was necessary to show that they were indeed located inside the cell.

The cytoplasm of the *Sulfolobus* cells appears to be densely packed. The density is homogeneous throughout the cells, and there are no regions of low density, as sometimes observed as an artifact in sectioned cells after chemical fixation and embedding at room temperature. As the intensity of the pixels in the reconstructed volume is proportional to the relative density, we can obtain a rough estimate for the protein concentration (more precisely, the total concentration of proteins and other biomolecules). We assume that the image intensity due to (hydrated) protein corresponds to the minimum intensity (maximum density) within a reconstructed slice. This can be obtained from the dark inclusion in Fig. 2 *C*, from the intensity of the S-layer boundaries, or from an analysis of the gray-value distribution within the cell. These values are only approximate, as the densities of lipid and protein are not equal, and as the composition of the inclusion is not known. All three measurements lead to similar results, however. The density of ice can be measured outside the cell. From these values and the mean intensity inside the cell, we obtain a protein concentration of 30–50%. As the calculation involves only relative intensities, we do not need to know any actual densities of the reconstructed volume. The obtained concentration is similar to the concentration measured by biochemical means for *Escherichia coli* cells, 0.3–0.4 g ml^{-1} (Zimmerman and Trach, 1991). It confirms that the in vivo concentration of protein is extremely high. The resulting close packing of the individual proteins makes their identification in electron tomographic sections difficult.

Tomography of *Pyrobaculum* cells was able to show the hexagonal array structure of the S-layer in three dimensions, meaning that a resolution significantly better than 30 nm was achieved for 300–500-nm-thick specimens. Even though this is not sufficient to identify single macromolecules, it may serve as an indication of the feasibility of localizing large macromolecular complexes in three dimensions in a not too crowded volume.

As whole cells are large structures offering information over a large size range, it would be convenient to use a larger detector like film for image recording. However, because of the limited dynamic range of this medium, it is generally unsuitable for specimens with thickness variations as large as those shown here, at least if contrast is enhanced by energy filtering. Application of higher accelerating voltages for the investigation of whole cells is mandatory, if structures larger than 1 μm in diameter are to be observed, to penetrate the specimen and to minimize multiple (elastic) scattering events. A higher accelerating voltage also leads to a substantially improved resolution for tomography as shown below. However, from the experience presented here, we believe that energy filtering is even more helpful for achieving a reasonable resolution.

The representation of three-dimensional crowded volumes poses a challenge by itself. If single molecules are to be visualized in cells as shown in Fig. 2, neither surface rendering nor volume rendering alone will be sufficient. It will be necessary to find a way of localizing the molecules, possibly by three-dimensional cross-correlations. As the molecules are randomly oriented in the volume, their cross section in slices through this volume may not be sufficient for detection and identification, except perhaps for highly symmetrical particles. In a final step, the particles would have to be isolated and visualized individually. Because of the dose restrictions it may even be that direct visual recognition of single molecules will not be possible, so that one has to rely on cross-correlation with a well-defined reference or on specific markers.

Estimation of the practical resolution limit of cryotomography

In addition to relatively poor contrast, the critical limitation for cryomicroscopy is the structural damage of the embedded sample due to the electron beam. The allowed dose differs from specimen to specimen. At 120 kV, it is roughly 2000 e nm^{-2} for high-resolution studies of single molecules and 6000 e nm^{-2} or more for studies at lower resolution. Visible bubble formation sets in at ~12,000–30,000 e nm^{-2} for the specimens shown in this study. The restriction of the allowed electron dose not only necessitates automation of tomographic procedures for ice-embedded specimens, it also fundamentally limits the obtainable resolution.

The parameters that have to be chosen for a tomographic series are the number of tilts and the tilt increment scheme, the exposure time for each image, the magnification, and the microscope defocus. The choice of each parameter is determined by the desired final resolution of the reconstruction.

Number of tilts and tilt scheme

According to Crowther et al. (1970) and Hoppe (1969), the resolution of a reconstruction, d, is determined by the tilt increment α_0, assuming equidistant sampling of the angular range:

$$d = D\alpha_0 \tag{1}$$

where D is the diameter of the specimen, and α_0 is given in radians. The effects introduced by the limited angular range (unavoidable in single-axis-tilt tomography) do not enter the calculations directly. The tilt increment is usually left unchanged throughout the tomographic series:

$$\alpha_{n+1} = \alpha_n + \alpha_0 \tag{2}$$

This sampling leads to an isotropic resolution only if the geometric thickness of the specimen is independent of the tilt angle (i.e., if the specimen is rod-shaped; Barnard et al., 1992), and if there is no missing wedge. In all other cases, the tilt increment should become smaller at high tilt angles, to "compensate" for the increasing specimen thickness. Even though different schemes for changing the tilt increment have been developed, the one by Saxton et al. (1984) has been most widely adapted. It will be referred to as the "Saxton scheme." The tilt angle varies as

$$\alpha_{n+1} = \alpha_n + \arcsin[\sin \alpha_0 \cos \alpha_n] \tag{3}$$

Equation 3 is slightly different from that given in a footnote in Saxton et al. (1984), because the authors used an approximation to the exact formula. The scheme was originally designed to leave the sampling distance at the resolution limit on a Cartesian grid in the z^* direction unchanged, which is especially desirable for crystalline specimens. The number of images in a tomographic series in terms of α_0 for the tilt range $\pm\alpha_{max}$ is

$$N = \left(2\frac{\alpha_{max}}{\alpha_0} + 1\right) \qquad \text{for constant increment} \tag{4}$$

$$N \approx \left(2\frac{\alpha_{max}}{\alpha_0} + 1\right)\frac{1}{2\alpha_{max}} \ln\frac{1 + \sin \alpha_{max}}{1 - \sin \alpha_{max}}$$

$$\text{approximated for the Saxton scheme} \tag{5}$$

For a tilt range of $\pm 60°$ and an initial increment of 1.5°, there are 81 images with constant increment and 99 images for the Saxton scheme. In the following, only the Saxton scheme will be considered. The maximum number of tilts used in practice is ~150, so that the duration of a series with 1.5 min per tilt angle is ~4 h (including some user interaction).

Exposure time

All images of a tomographic series should ideally have a similar SNR. As the specimen thickness in the beam direction generally increases with the tilt angle, the exposure time should also be increased. If this is not done, the images at high tilt angles show an insufficient SNR, or the images at low tilt have an unnecessarily high SNR, thereby "wasting" the electron dose. The most useful schemes for varying the exposure time are

$$t = t_0 \qquad \text{"constant"} \tag{6}$$

$$t = t_0 \exp[T(1/\cos \alpha - 1)] \qquad \text{"exp"} \tag{7}$$

$$t = t_0/\cos \alpha \qquad \text{"cos"} \tag{8}$$

where $T = D/\Lambda$, D is the specimen thickness at 0° tilt, and Λ is the effective mean free path. The relative exposure time t/t_0 for the three cases is displayed in Fig. 6, in the "exp" case for several values of T as parameter. For the reconstruction, the images have to be normalized with respect to the exposure time, so that the incident beam dose becomes nominally the same for all tilt angles. The "exp" scheme is designed to keep the count rate on the detector, and thereby the SNR, constant in all images of a specimen of constant thickness. The effective mean free path in this case is an empirical mean free path that depends on the particular objective aperture used. In the case of an energy-filtering microscope, it is approximately the inelastic mean free path, for which a value of 200 nm (350 nm) is used in the following for 120 kV (300 kV) electrons (Grimm et al., 1996b). As inelastically scattered electrons do not carry high-resolution information, the same values should be used for resolution estimation, even without energy filtering. The thickness of the specimen is only known with limited accuracy beforehand, and possibly is not constant over the field of view, so that a constant SNR cannot be achieved in practice. In the case of whole cells in thin ice, the "cos" scheme has proved to be useful. At 60°, the relative exposure time for the "cos" scheme is 2, whereas it is 1.6 (2.7/7.4/20/55) for the "exp" scheme for a 100-nm (200 nm/400 nm/600 nm/800 nm)-thick specimen at 120 kV. If the longest exposure time due to the stability of the cryoholder is 2 s, the shortest useful exposure time of a CCD

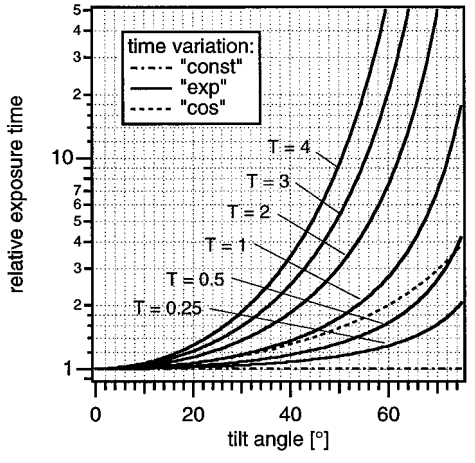

FIGURE 6 Relative exposure time t/t_0 for the different time variation schemes (Eqs. 6–8) and a tilt range up to 75°.

camera (used for tracking) is ~0.005 s, and the exposure for image acquisition is at least 10 times this value, one obtains a factor of 40. Another limitation is the brightness of the electron gun, i.e., whether enough electrons can pass the specimen to produce a significant signal on the detector in such a short period of time. In any case, it is necessary to require a minimum count rate on the detector for an SNR that is sufficient for marker alignment of the individual images. It was chosen as $p = 5$ e/pixel from practical experience ($p = 2$ e/pixel will also be investigated). This results in the minimum dose for the untilted image, so that the total dose of a series can be calculated from the sum over all exposure times during the series.

Magnification and defocus

The nominal resolution of a CCD image is twice the pixel size on the specimen level. Because of an insufficient transfer function (MTF) of the CCD camera, it is often advisable to reconstruct only up to a 2×2 binned resolution, corresponding to a $2\times$ oversampling: $os = 2$ (the case $os = 1$ will also be investigated). This, in turn, allows to us set the defocus to higher values, i.e., the first zero of the CTF can be chosen to be at half the Nyquist frequency, thereby increasing image contrast as compared to imaging without oversampling.

Estimation of the resolution

Building the above assumptions (five electrons per pixel and 200 nm (350 nm) mean free path at 120 kV (300 kV)) into a simulation, one can calculate all necessary quantities to estimate the achievable resolution at a given dose. The basic tilt increment is determined from the specimen thickness and the required resolution, as given by the Crowther criterion (Eq. 1). The required resolution, together with the given oversampling factor, determines the magnification. The magnification, in combination with the required count rate per pixel, yields the dose needed for the untilted image. In this calculation it is important to consider the exponential attenuation of the incident beam due to inelastic scattering in the specimen. The dose for the reconstruction is then computed iteratively, summing all exposure times at all tilt angles and multiplying by the dose at 0° tilt angle. The necessary dose for a given resolution in the reconstruction is shown in Fig. 7. At the voltages of 120 kV and 300 kV, which are currently used for low-dose tomography, both cases assume zero-loss energy filtering. Whereas 300 kV instruments have so far mainly been used for homogeneously thick specimens, so that the "exp" time increment scheme should be chosen, tomography of whole cells in thin ice, for which the "cos" time increment scheme is advantageous, has only been performed on a 120-kV instrument. The tilt range of ±60° is currently the standard for beam-sensitive specimens. The range of ±70° requires substantially more dose, but the gain in resolution is not formally described by the Crowther criterion (for a discussion of the dependence of resolution on the tilt range, see the book by Frank (1992)). The ±70° range has been evaluated only for 300 kV. To be able to directly compare the different accelerating voltages, the equivalent dose, which is proportional to β^2 ($\beta = v/c$ is the ratio of the electron velocity to the

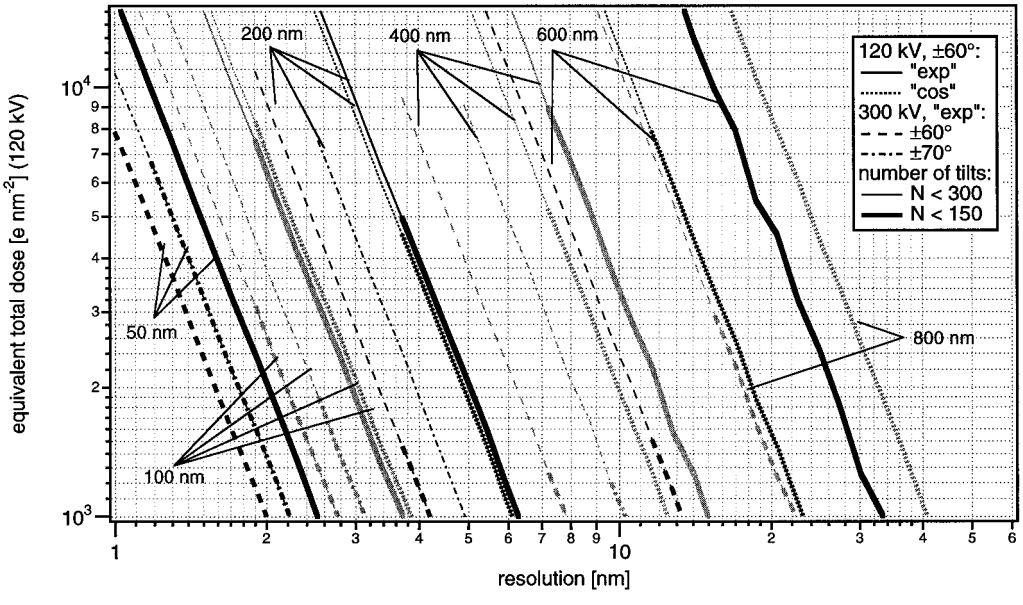

FIGURE 7 Total dose in electron tomography, using accelerating voltages of 120 kV or 300 kV, with zero-loss energy filtering, as a function of resolution. Four cases are shown for six specimens of different thickness. For 120-kV accelerating voltage, the exposure time is varied according to the "exp" scheme and the "cos" scheme (Eqs. 7 and 8), with an angular range of ±60°. For 300 kV, the "exp" scheme is assumed, and the dose with an angular range of ±60° and ±70° is shown. The cases where the total number of images is below 150 are shown with thick lines. Fine lines indicate a total number between 150 and 300. The Saxton tilt angle increment scheme was chosen in all cases. $p = 5$ and $os = 2$.

speed of light), has been chosen for plotting instead of the absolute electron dose. A factor of 1.75 more electrons are allowed at 300 kV as compared to 120 kV, because of the larger mean free path lengths. In all cases, the total dose is proportional to d^{-3}, as observed in Fig. 7. The attainable resolution for a given set of parameters varies by a factor of somewhat more than 2 for a change in dose by a factor of 10. This means that there is little use in increasing the total dose and thereby risking the structural preservation of the sample when thin specimens are investigated at high resolution. For thick specimens, the loss in resolution due to beam damage will in most cases be smaller than the gain in resolution due to the increased electron dose. It is interesting to note that in the shown range in the figure it is not possible at all to image samples 600 nm and thicker with a ±70° angular range at 300 kV using the "exp" time variation, or 800-nm-thick samples with ±60° angular range at 120 kV.

For a given initial tilt increment α_0, corresponding to a certain thickness, the number of images in a series depends only on the angular range. The resulting resolution can be attained with a 300-kV instrument with less dose than at 120 kV. For a thickness of more than 100 nm and a dose of 2000 e nm^{-2}, with a 300-kV instrument one always needs to record more than 150 images for the resolution shown in Fig. 7. If the dose is limited to 8000 e nm^{-2}, no more than 300 views are needed.

To be able to better compare the resolution obtained for the four different cases, it was plotted against the specimen thickness for a fixed dose of 6000 e nm^{-2} in Fig. 8 *A*. In general, the resolution limit increases exponentially for a specimen thickness greater than ~200 nm. The difference in the resolution for the cases illustrated becomes small for a thickness of less than 100 nm. The case with the "cos" time variation scheme cannot be directly compared with the others, as it represents a different specimen geometry. For specimens of a thickness that allows using this time variation scheme, the obtained resolution can be significantly better than in the case of a homogeneously thick specimen. However, for an 800-nm-thick sample, the resolution is still worse than 20 nm in this case (for Fig. 8, no limit has been set for the relative exposure time). The most important question is whether the resolution necessary for the detection of single macromolecules can be achieved for a given specimen. At 120 kV, 10-nm resolution can be obtained for specimens up to 440 nm thickness, whereas the specimen must not be thicker than 220 nm for 4-nm resolution and 100 nm for 2-nm resolution. Identification of individual molecules, using their shape as a signature, requires a resolution of 2–4 nm, whereas large structures such as S-layer stalks can be seen because of their periodic arrangement, even at 10 nm resolution. At 300 kV, the corresponding thicknesses for 2-nm, 4-nm, and 10-nm resolution are 150, 360, and 700 nm, respectively. The gain by the higher accelerating voltage due to the higher mean free path and due to the increased allowable dose is therefore substantial.

Fig. 8 *B* shows the resolution for ±60° and the "exp" time variation scheme for the two voltages and for three

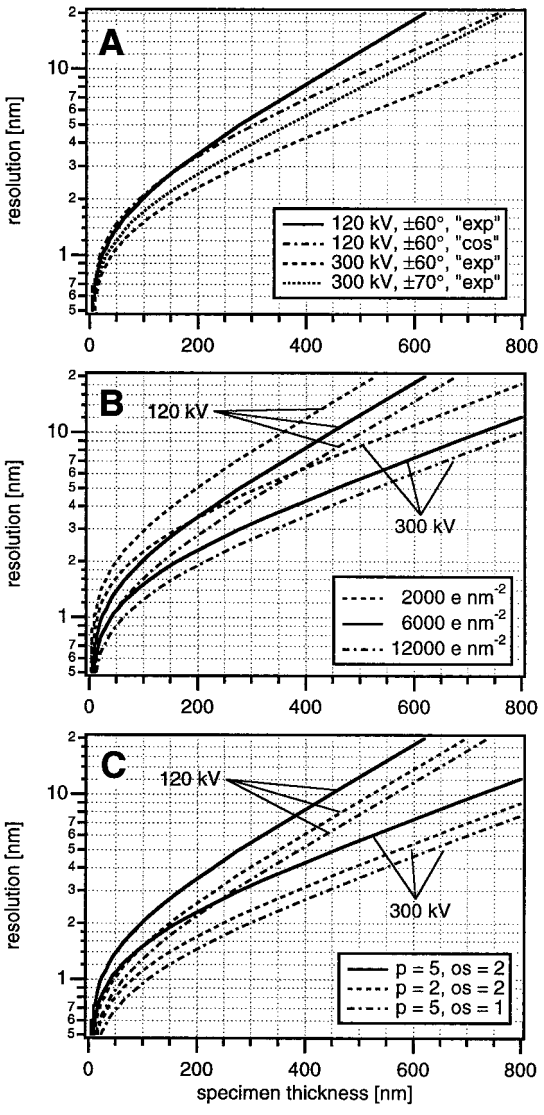

FIGURE 8 Attainable resolution as a function of the specimen thickness (*A*) for the cases from Fig. 7. The electron dose was 6000*e* nm^{-2}; (*B*) for three different dose limits with an angular range of ±60° and the "exp" increment for the exposure time; (*C*) for two different minimum count rates per pixel and two oversampling factors, ±60° tilt range, 6000*e* nm^{-2} dose limit, and the "exp" increment scheme.

different dose limits. Compared with the values for 6000 e nm^{-2}, the same resolution can be obtained for specimens that are thicker (thinner) by a fixed amount if 12,000 e nm^{-2} (2000 e nm^{-2}) is used. The shift is 60 nm (−90 nm) for 120 kV and 90 nm (−130 nm) for 300 kV at a dose of 12,000 e nm^{-2} (2000 e nm^{-2}) (thickness greater than 100 nm).

Fig. 8 *C* shows the resolution for the two accelerating voltages at 6000 e nm^{-2} if the restrictions on the required number of electrons per pixel or the oversampling on the CCD camera are changed. This illustrates the order of magnitude of the changes. As the calculations are in any case idealized, it should be assumed that resolutions in actual reconstructions may be worse by a factor of up to ~5, as inferred from our practical experience so far.

CONCLUSIONS

Using the constraint that five electrons per pixel should be available in every projection, the resolution that can be attained in a tomographic reconstruction has been calculated depending on the specimen thickness and on the accelerating voltage used. If specimens thicker than 100 nm are investigated, a total number between 100 and 300 views is required to obtain the optimum resolution. Identification of single macromolecules, which requires a resolution of 2–4 nm, is only feasible in specimens thinner than 200 nm (350 nm) at 120 kV (300 kV). Useful low-resolution reconstructions (~10 nm) are possible with specimens up to 450 nm (700 nm) thick. These values are calculated on a theoretical basis and certainly have to be corrected for real tomography, because of the nonideal use of electrons for imaging, the additional dose needed for the automation of tomographic procedures, and artifacts introduced by the missing wedge. The experimental reconstructions shown had a resolution that was worse by a factor of 2–5. This is probably due to the fact that neither the chosen magnification nor the dose per image was truly optimized yet. The given numbers correspond to angular ranges of $\pm 60°$ and $\pm 70°$.

Other microscopies, i.e., confocal microscopy and particularly x-ray microscopy, are also being continuously developed toward higher resolution. These techniques are able, at least in principle, to image structures up to several microns in thickness in a hydrated state. Although the resolution of conventional confocal microscopy is limited to ~200 nm in the *x-y* plane and 400 in the *z* direction, recently 4π-confocal microscopy has reached a resolution better than 100 nm in all directions (Hell et al., 1997). X-ray microscopy, like electron microscopy, is largely limited by specimen damage due to the penetrating beam. Cryofixation of the specimen will result in a decreased sensitivity and will prevent specimen motion if tomographic techniques are applied (Methe et al., 1998). With a current 3D resolution of ~100 nm on beam-insensitive specimens, one may eventually be able to reach 30–50 nm for biological specimens (Kirz et al., 1995; Sayre and Chapman, 1995). Even though the damage produced in the specimen for a certain signal is higher for x-rays than for electrons, x-rays are advantageous for imaging specimens in thick (>1 μm) layers of water or ice. This is due to the presence of the "water window," in which the penetration distance through water is about an order of magnitude larger than in organic material. This leads to higher contrast as compared to electron microscopy, however at significantly lower resolution.

Is electron cryotomography worthwhile? The answer is generally yes. Electron tomography is able to attain resolutions necessary for macromolecular studies in specimens of up to ~400 nm thickness. It thereby opens access to cellular structures at a resolution that cannot be attained by other methods. As good resolution is only available for relatively thin objects and many cellular structures are much larger than 400 nm, cryosectioning instead of plunge-freezing of whole cells will be the technique of choice. For specimens thicker than 400 nm, the resolution of the reconstructions is too low to take full advantage of the better structural preservation by ice-embedding. When single macromolecules are investigated, electron tomography can be performed in conjunction with averaging (Nitsch et al., manuscript submitted for publication). Thus far in this case, other single-particle reconstruction schemes have the advantage of experimental simplicity.

The authors thank Gertraud Rieger for cultivating the Pyrobaculum cells.

This research was supported by the Deutsche Forschungsgemeinschaft (Ty 2/4-2).

REFERENCES

Barnard, D. P., J. N. Turner, J. Frank, and B. F. McEwen. 1992. A 360° single-axis tilt stage for the high-voltage electron microscope. *J. Microsc.* 167:39–48.

Baumeister, W., I. Wildhaber, and B. M. Phipps. 1989. Principles of organization in eubacterial and archaebacterial surface proteins. *Can. J. Microbiol.* 35:215–227.

Braunfeld, M. B., A. J. Koster, J. W. Sedat, and D. A. Agard. 1994. Cryo automated electron tomography: towards high-resolution reconstructions of plastic embedded structures. *J. Microsc.* 174:75–84.

Brock, T. D., K. M. Brock, R. T. Belly, and R. L. Weiss. 1972. Sulfolobus: a new genus of sulfur-oxidizing bacteria living at low pH and high temperature. *Arch. Microbiol.* 84:54–68.

Crowther, R. A., D. J. DeRosier, and A. Klug. 1970. The reconstruction of a three-dimensional structure from its projections and its applications to electron microscopy. *Proc. R. Soc. Lond.* 317:319–340.

de Jong, A. F., J. Rees, W. M. Busing, and U. Lücken. 1996. Integrated energy-filtering TEM—the CM120-Biofilter. *Prog. Biophys. Mol. Biol.* 65:H116–H116.

Dierksen, K., D. Typke, R. Hegerl, and W. Baumeister. 1993. Towards automatic electron tomography. II. Implementation of autofocus and low-dose procedures. *Ultramicroscopy.* 49:109–120.

Dierksen, K., D. Typke, R. Hegerl, A. J. Koster, and W. Baumeister. 1992. Towards automatic electron tomography. *Ultramicroscopy.* 40:71–87.

Dierksen, K., D. Typke, R. Hegerl, J. Walz, E. Sackmann, and W. Baumeister. 1995. Three-dimensional structure of lipid vesicles embedded in vitreous ice and investigated by automated electron tomography. *Biophys. J.* 68:1416–1422.

Dubochet, J., M. Adrian, J. Chang, J.-C. Homo, J. Lepault, A. W. McDowall, and P. Schultz. 1988. Cryo-electron microscopy of vitrified specimens. *Q. Rev. Biophys.* 21:129–228.

Frank, J. 1992. Electron Tomography. Plenum Press. New York.

Grimm, R., M. Bärmann, W. Häckl, D. Typke, E. Sackmann, and W. Baumeister. 1997. Energy-filtered electron tomography of ice-embedded actin and vesicles. *Biophys. J.* 72:482–489.

Grimm, R., A. J. Koster, U. Ziese, D. Typke, and W. Baumeister. 1996a. Zero-loss energy-filtering under low-dose conditions using a postcolumn energy filter. *J. Microsc.* 183:60–68.

Grimm, R., D. Typke, M. Bärmann, and W. Baumeister. 1996b. Determination of the inelastic mean free-path in ice by examination of tilted vesicles and automated most probable loss imaging. *Ultramicroscopy.* 63:169–179.

Han, K. F., A. J. Gubbens, J. W. Sedat, and D. A. Agard. 1996. Optimal strategies for imaging thick biological specimens—exit wave-front reconstruction and energy-filtered imaging. *J. Microsc.* 183:124–132.

Hegerl, R. 1996. The EM program package: a platform for image processing in biological electron microscopy. *J. Struct. Biol.* 116:30–34.

Hell, S. W., M. Schrader, and H. T. M. van der Voort. 1997. Far-field fluorescence microscopy with three dimensional resolution in the 100-nm range. *J. Microsc.* 187:1–7.

Hoppe, W. 1969. Das Endlichkeitspostulat und das Interpolationstheorem der dreidimensionalen elektronenmikroskopischen Analyse aperiodischer Strukturen. *Optik.* 29:617–621.

Kirz, J., C. Jacobsen, and M. Howells. 1995. Soft x-ray microscopes and their biological applications. *Q. Rev. Biophys.* 28:33–130.

Koster, A. J., H. Chen, J. W. Sedat, and D. Agard. 1992. Automated microscopy for electron tomography. *Ultramicroscopy.* 46:207–227.

Krivanek, O. L., S. L. Friedman, A. J. Gubbens, and B. Kraus. 1995. An imaging filter for biological applications. *Ultramicroscopy.* 59:267–282.

Langmore, J. P., and M. F. Smith. 1992. Quantitative energy-filtered electron microscopy of biological molecules in ice. *Ultramicroscopy.* 46:349–373.

Mannella, C. A., M. Marko, P. Penczek, D. Barnard, and J. Frank. 1994. The internal compartmentation of rat-liver mitochondria: tomographic study using the high-voltage transmission electron microscope. *Microsc. Res. Tech.* 27:278–283.

McEwen, B. F., K. H. Downing, and R. M. Glaeser. 1995. The relevance of dose-fractionation in tomography of radiation-sensitive specimens. *Ultramicroscopy.* 60:357–373.

Methe, O., H. Spring, P. Guttmann, G. Schneider, D. Rudolph, M. F. Trendelenburg, and G. Schmahl. 1998. Transmission x-ray microscopy of intact hydrated PTK2 cells during the cell cycle. *J. Microsc.* (in press).

Moritz, M., M. B. Braunfeld, J. W. Sedat, B. Alberts, and D. A. Agard. 1995. Microtubule nucleation by gamma-tubulin-containing rings in the centrosome. *Nature.* 378:638–640.

Olins, A. L., D. E. Olins, H. A. Levy, S. M. Margle, E. P. Tinnel, and R. C. Durfee. 1989. Tomographic reconstruction from energy-filtered images of thick biological sections. *J. Microsc.* 154:257–265.

Perkins, G., C. Renken, M. E. Martone, S. J. Young, and M. Ellisman. 1997. Electron tomography of neuronal mitochondria—3-dimensional structure and organization of cristae and membrane contacts. *J. Struct. Biology.* 119:260–272.

Phipps, B. M., H. Engelhardt, R. Huber, and W. Baumeister. 1990. Three-dimensional structure of the crystalline protein envelope layer of the hyperthermophilic archaebacterium *Pyrobaculum islandicum. J. Struct. Biol.* 103:152–163.

Phipps, B. M., R. Huber, and W. Baumeister. 1991. The cell envelope of the hyperthermophilic archaebacterium *Pyrobaculum organotrophum* consists of two regularly arrayed protein layers: three-dimensional structure of the outer layer. *Mol. Microbiol.* 5:253–265.

Saxton, W. O., W. Baumeister, and M. Hahn. 1984. The three-dimensional reconstruction of imperfect two-dimensional crystals. *Ultramicroscopy.* 13:57–70.

Sayre, D., and H. N. Chapman. 1995. X-ray microscopy. *Acta Crystallogr. A.* 51:237–252.

Schleper, C., I. Holz, A. Janekovic, J. Murphy, and W. Zillig. 1995. A multicopy plasmid of the extremely thermophilic archeon *Sulfolobus* effects its transfer to recipients by mating. *J. Bacteriol.* 177:4417–4426.

Schröder, R. R., W. Hofmann, and J.-F. Ménétret. 1990. Zero-loss energy filtering as improved imaging mode in cryoelectronmicroscopy of frozen-hydrated specimens. *J. Struct. Biol.* 105:28–34.

Shillito, B., A. J. Koster, J. Walz, and W. Baumeister. 1997. Electron tomographic reconstruction of plastic-embedded organelles involved in the chitin secretion process. *Biol. Cell.* 88:5–13.

Völkl, P., R. Huber, E. Drobner, R. Rachel, S. Burggraf, A. Trincone, and K. O. Stetter. 1993. Pyrobaculum aerophilum sp. nov., a novel nitrate-reducing hyperthermophilic archeum. *Appl. Environ. Microbiol.* 59: 2918–2928.

Zimmerman, S. B., and S. O. Trach. 1991. Estimation of macromolecule concentrations and excluded volume effects for the cytoplasm of *Escherichia coli. J. Mol. Biol.* 222:599–620.